ACS APPLIED NANO MATERIALS

www.acsanm.org Article

Rapid Laser Pulse Synthesis of Supported Metal Nanoclusters with Kinetically Tunable Size and Surface Density for Electrocatalytic Hydrogen Evolution

Yong Yang, Yonggang Yao, Dylan J. Kline, Tangyuan Li, Pankaj Ghildiyal, Haiyang Wang, Liangbing Hu,* and Michael R. Zachariah*

Cite This: *ACS Appl. Nano Mater.* 2020, 3, 2959−2968 Read Online

ACCESS | Metrics & More | Article Recommendations | Supporting Information

ABSTRACT: Matrix-supported metal nanoclusters (1−10 nm) with unique size- and shape-dependent properties have drawn attention for their potential applications in electronics, catalysis, energy storage, and sensors. However, synthesis of matrix-supported ultrasmall nanoclusters at high concentration and in an unaggregated state is challenging. Here we demonstrate a rapid laser pulse technique to *in situ* fabricate ultrasmall metal nanoclusters supported on a carbon nanofiber (CNF) matrix with kinetically controllable size and surface density. A rapid laser pulse heating on the metal precursor incorporated CNF matrix triggers the fast nucleation and growth of metal nanoclusters, and a subsequent ultrafast quenching freezes them onto the CNF structure. We find that a shorter laser pulse enables the formation of metal nanoclusters with higher number densities and smaller sizes while longer laser pulse leads to the further growth of metal nanoclusters and the achievement of their equilibrium shape. A characteristic time analysis suggests that the growth of metal nanoclusters is dominated by surface diffusion and sintering, and Ostwald ripening is mainly involved at the early stage of nanocluster formation. We also demonstrate that the catalytic performance of CNF matrix supported metal nanoclusters toward electrocatalytic hydrogen evolution is enhanced for metal nanoclusters with a smaller size and higher number density. This work provides a promising approach for rapid and scalable fabrication of ultrasmall, high-density metal nanoclusters, and nanocluster-based devices.

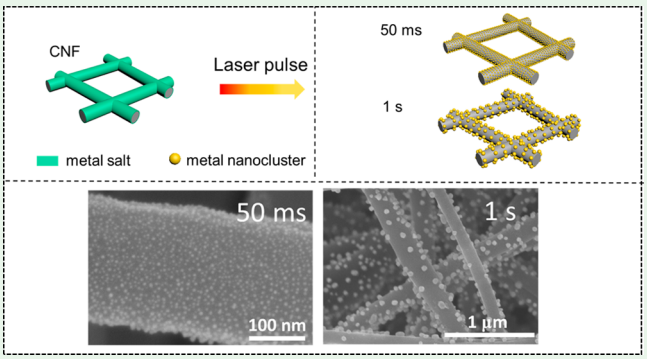

KEYWORDS: *supported metal nanoclusters, laser pulse, growth mechanism, nanomanufacturing, laser fabrication*

1. INTRODUCTION

Matrix-supported metal nanoclusters (1−10 nm) have shown potential for applications in electronics, catalysis, energy storage, and sensors.[1−3] Although many techniques have been developed to decorate metal nanoclusters onto the supporting matrices,[4] achieving a higher surface density while maintaining an ultrasmall size and uniform dispersity is extremely difficult because of the metastable nature and the rapid aggregation of nanoclusters. Simply increasing the nanocluster surface density by adding more nanoclusters onto the host matrix often leads to nanocluster aggregation, uneven dispersion, and further growth of nanoclusters into larger sizes. In addition, most of those reported techniques only produce supported nanoclusters in small quantities and are therefore not suitable for immediate technological applications. Hence, there is a need to develop an effective, facile, and industrially scalable technique to synthesize supported metal nanoclusters with an ultrasmall size and extremely high surface density.

From a thermodynamic standpoint, one strategy to produce nanoclusters with a smaller size and a higher number density is to promote nucleation and simultaneously limit growth. This can be achieved by employing a fast thermal pulse to rapidly decompose the metal precursor to create a highly supersaturated state, leading to a fast nucleation burst. Subsequent rapid cooling can then quench the growth of small nuclei and form ultrasmall nanoclusters. Recently, we demonstrated a thermal pulse technique to generate high-surface-density, ultrasmall metal nanoclusters and nanoalloys decorated on carbon nanofiber thin films.[5,6] Rapid heating and fast nanocluster formation were achieved by electrically heating a conductive carbon matrix. Despite being an rapid technique,

Received: January 28, 2020
Accepted: February 4, 2020
Published: February 4, 2020

Downloaded via UNIV OF CALIFORNIA RIVERSIDE on December 9, 2020 at 19:11:56 (UTC).
See https://pubs.acs.org/sharingguidelines for options on how to legitimately share published articles.

ACS Publications © 2020 American Chemical Society

https://dx.doi.org/10.1021/acsanm.0c00238
ACS Appl. Nano Mater. 2020, 3, 2959−2968

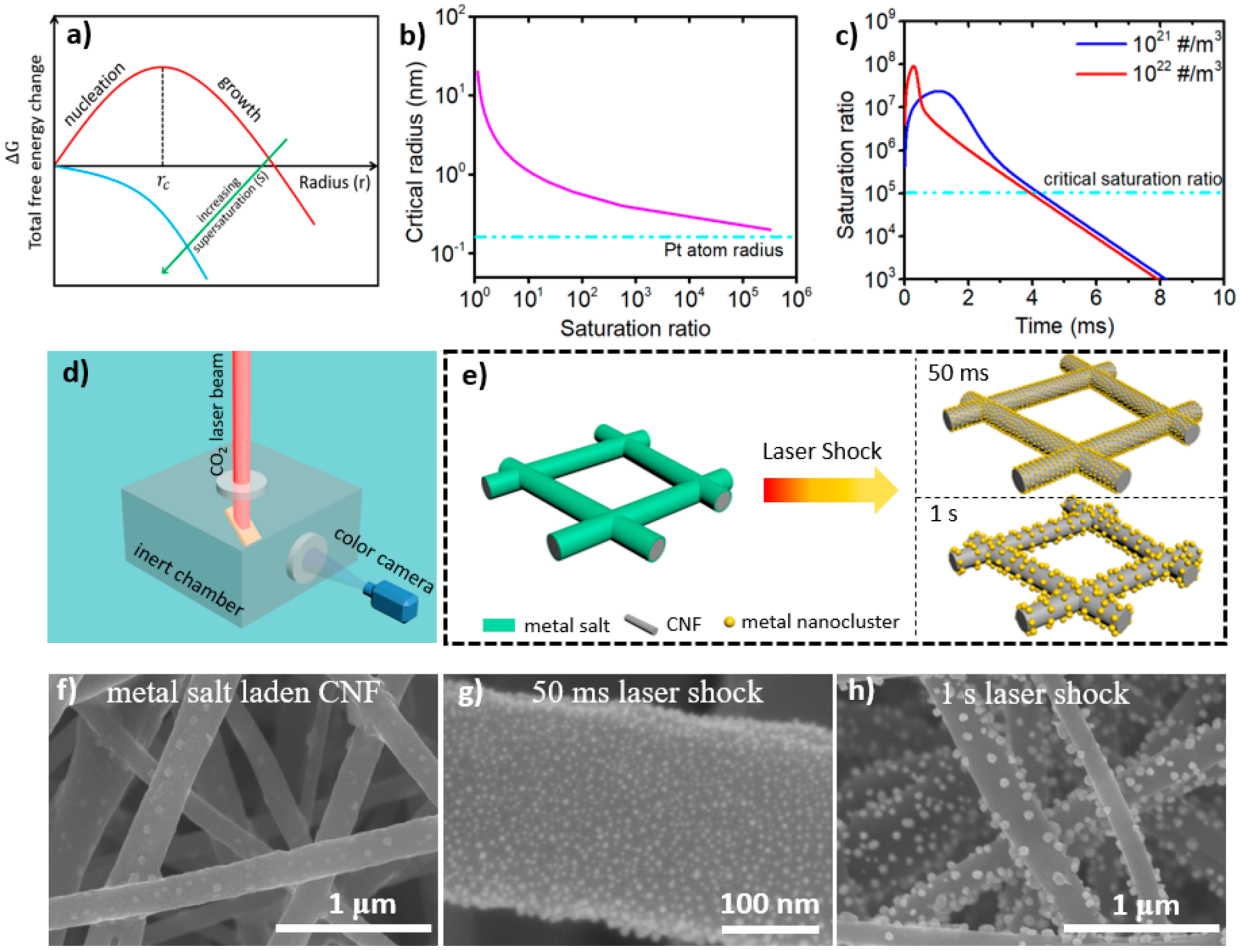

Figure 1. Laser-induced thermal pulse technique for nanocluster synthesis. (a−c) Relationship between the critical nucleus radius and the saturation ratio of metal atoms. (d) Schematic of apparatus. (e) Effect of laser pulse duration on nanocluster size and number density. (f) SEM image of H_2PtCl_6-coated CNF film. (g, h) CNF supported Pt nanoclusters synthesized by 50 ms and 1 s laser pulses, respectively.

this Joule heating-assisted thermal pulse technique is limited to electrically conductive matrices and is not amenable to bulk production of supported ultrasmall nanoclusters with high surface densities.

Lasers present a flexible and powerful nanomanufacturing approach to provide both temporally and spatially resolved energy to generate nanoclusters.[7,8] Laser-based manufacturing approaches shift the control and modulation of properties from the material to a programmable source, making them readily adaptable to industrial protocols. Laser approaches to nanomaterial fabrication become especially consequential as we adapt to emerging manufacturing approaches like 3-D printing and writing.[9,10] In recent years, a number of laser techniques have attracted tremendous research interest, including laser-induced dewetting of thin films laser synthesis and processing of colloids (LSPC) and laser direct synthesis and patterning (LDSP).[7,8,10−12] Laser-induced dewetting techniques, in particular, have recently demonstrated high precision, control, and scalability in the generation of large metal nanoparticle ensembles from metallic thin films.[11−14] However, these approaches have not been expanded to metal nanocluster formation in the sub-10 nm regime on high-surface-area matrices. Previous studies have explored metal nanoparticle decoration on multiwalled carbon nanotubes by laser ablation of metal nanoparticles and carbon nanotubes in aqueous media.[15] However, nanoparticles decorated this way are severely agglomerated and have low surface density on the matrix surface. In addition, the process is tedious, and tunability of particle size and properties is quite complex.

In this work, we demonstrate a fast, thermal pulse technique using a commercial CO_2 laser as the heating source to introduce an extremely short laser pulse to trigger the formation of ultrasmall, dense, and uniformly dispersed metal nanoclusters on carbon nanofiber matrices. This approach is a facile way to precisely tune nanocluster size, surface density, and shape. We observe that a shorter laser pulse enables the formation of smaller nanoclusters with high number densities. Conversely, a longer laser pulse leads to the further growth of metal nanoclusters and the achievement of their equilibrium shape. A characteristic time analysis suggests that the growth of metal nanoclusters is primarily dominated by coagulation and sintering, with Ostwald ripening mainly involved at the early stage of nanoparticle formation. As an example application, we demonstrate size-dependent catalytic properties of Pt nanoclusters for electrocatalytic hydrogen evolution. This further demonstrates the ability of this approach for an easy and fast tuning of material properties through a simple modulation of laser parameters. This technique represents a promising approach for rapid and scalable fabrication of tunable, ultrasmall, high-density metal nanoclusters and nanocluster-based devices.

https://dx.doi.org/10.1021/acsanm.0c00238
ACS Appl. Nano Mater. 2020, 3, 2959−2968

2. RESULTS AND DISCUSSION

Thermodynamic and Kinetic Criteria. Here, we first use classical nucleation theory to investigate if a rapid laser pulse can produce a supersaturated metal atom vapor condition for a fast nucleation burst and nanocluster formation. Thermodynamically, a nucleation process can be described by the Gibbs free energy droplet model,[16] where the critical radius, r_c, of a stable nucleus is expressed as

$$r_c = \frac{2\sigma V_m}{RT \ln S} \tag{1}$$

Here, S is the saturation ratio of the Pt vapor, σ is the surface tension of Pt nanoclusters in the liquid phase, and V_m is the molar volume of bulk metallic Pt. Equation 1 indicates that increasing the saturation ratio S of Pt vapor decreases the critical radius of the nanoclusters (Figure 1a), assuming a size-independent surface and constant temperature. In an extreme case, we can imagine a saturation ratio high enough to cause each single atom to become a stable nucleus. Figure 1b shows that this scenario becomes feasible when $S > 10^5$, when the critical radius approaches the radius of a platinum single atom (~0.2 nm). Ideally, creating a highly saturated condition for metal atoms in a short time should allow a fast nucleation and formation of stable nuclei with an ultrasmall size. A subsequent fast cooling step would then freeze and stabilize these clusters onto a host matrix with high density and dispersity.

We examine whether a CO_2 laser is fast enough to create such high saturation ratios in an extremely short time. To estimate these time scales, a crucial parameter to consider is the saturation ratio change of the monomer (Pt atoms) in the CNF matrix during laser pulse heating. This saturation ratio change is mainly affected by four primary processes: (a) generation of Pt atoms from thermal decomposition of H_2PtCl_6, (b) consumption of Pt atoms due to nucleus formation, (c) evaporation of Pt atoms from the surface of the stable nuclei, and (d) consumption of vapor phase Pt atoms due to Pt condensation onto the surface of the existing nuclei. These processes can be well described by the moment model as follows:[17,18]

$$\frac{dS}{dt} = \frac{R_H}{n_s} - \frac{Jk^*}{n_s} - (S-1)\frac{B_1 A}{2v_1 n_s} \tag{2}$$

Here, R_H is the reaction rate of metal salt precursor decomposition to zerovalent metal atoms, and A is the total surface area of all the nuclei in the reaction volume; both R_H and A are time-dependent variables. k^* is the number of monomers in a single particle with a critical radius r_c, and n_s is the monomer concentration at saturation condition. $B_1 = 2n_1 v_1 \left(\frac{kT}{2\pi m_1}\right)^{1/2}$, where n_1 is the monomer number concentration; v_1 and m_1 are the volume and mass of the monomer, respectively; J is the rate of particle formation by the nucleation. For a homogeneous nucleation process, J is given as follows:[17]

$$J_{homo} = \frac{Kn_1 s_1}{3}\sqrt{\frac{\Phi}{\pi}} \exp\left(-\frac{4}{27}\frac{\Phi^3}{(\ln S)^2}\right) \tag{3}$$

where $K = n_1\left(\frac{kT}{2\pi m_1}\right)^{1/2}$, Φ is dimensionless surface tension of the stable nuclei, $\Phi = \frac{s_1\sigma}{kT}$; s_1 is the surface area of a monomer. However, the presence of the carbon nanofibers would be expected to further lower the nucleation barrier and promote heterogeneous nucleation, which can be expressed as[19]

$$J_{hetero} = \frac{Kn_1 s_1}{3}\sqrt{\frac{\Phi}{\pi}} \exp\left(-\frac{4}{27}\frac{\Phi^3}{(\ln S)^2}\right) f(\theta) \tag{4}$$

where $f(\theta) = 1/4(2 + \cos\theta)(1 - \cos\theta)^2$, which is the reduction factor and θ is the contact angle between the metal and carbon surface. Therefore, we use J_{hetero} in eq 2 for the saturation ratio calculation. The values for all the property parameters and the details of the calculation can be found in the Supporting Information.

Figure 1c shows the calculated change in saturation ratio of Pt atoms with the duration of the laser pulse. We see that for two metal precursor loadings investigated (10^{21} and 10^{22} #/m^3) a short laser pulse is fast enough to create a supersaturated state ($S > 10^5$) of Pt atoms, enabling a rapid nucleation burst and formation of extremely small nanoclusters which are also thermodynamically favorable. Note that particle coagulation and particle sintering are not considered in the calculation, and the role of coagulation and sintering on nanoparticle growth will be discussed later.

Laser-Induced Thermal Pulse Technique. Figure 1d shows the experimental system for the laser pulse technique fabrication of carbon nanofiber supported metal nanoclusters. Pt nanoclusters were chosen as the model system to investigate the process−structure relationship. In a typical experiment, the metal precursor was impregnated onto carbon nanofibers by depositing the precursor solution onto a carbon nanofiber thin film. After drying at ambient conditions, the metal precursor impregnated CNF thin film sample was mounted onto a custom graphite substrate located in the center of an inert Ar gas-filled chamber. The photothermal pulse on the thin film sample was performed by using a CO_2 laser (SYNRAD, ti series) operating at 10.6 μm with an output power of 70 W. The heating process was recorded by a high-speed color camera (Vision Research Phantom Micro), and a spatiotemporal temperature map of the thin film sample was obtained based on the recorded camera video.[20] A pulse generator was used to simultaneously trigger the CO_2 laser beam irradiation and the high-speed camera recording process.

Figure 1e shows a schematic of synthesis of CNF supported metal nanoclusters by the laser pulse technique. A surface layer of metal salt precursor is uniformly coated on the carbon nanofiber matrix. Laser pulse heating triggers rapid thermal decomposition of the metal salt and subsequent nucleation of metal nanoclusters. Fast quenching stabilizes these small nanoclusters on the surface of the carbon nanofiber matrix and prevents further growth. By simply controlling the duration of the laser pulse, one can synthesize metal nanocluster with tunable size and surface density. As shown in Figure 1e, a shorter laser pulse leads to formation of smaller nanoclusters (represented by gold color spheres) with a higher surface number density. On the other hand, a longer laser pulse promotes further nanocluster growth, resulting in the formation of large-size particles with a lower surface number density.

The microstructure evolution of supported Pt nanoclusters carbon nanofibers before and after the laser pulse treatment was investigated by using scanning electron microscopy. Figure 1f shows a uniform coating of the metal precursor (H_2PtCl_6) on the surface of carbon nanofibers. The incident high-power

https://dx.doi.org/10.1021/acsanm.0c00238
ACS Appl. Nano Mater. 2020, 3, 2959−2968

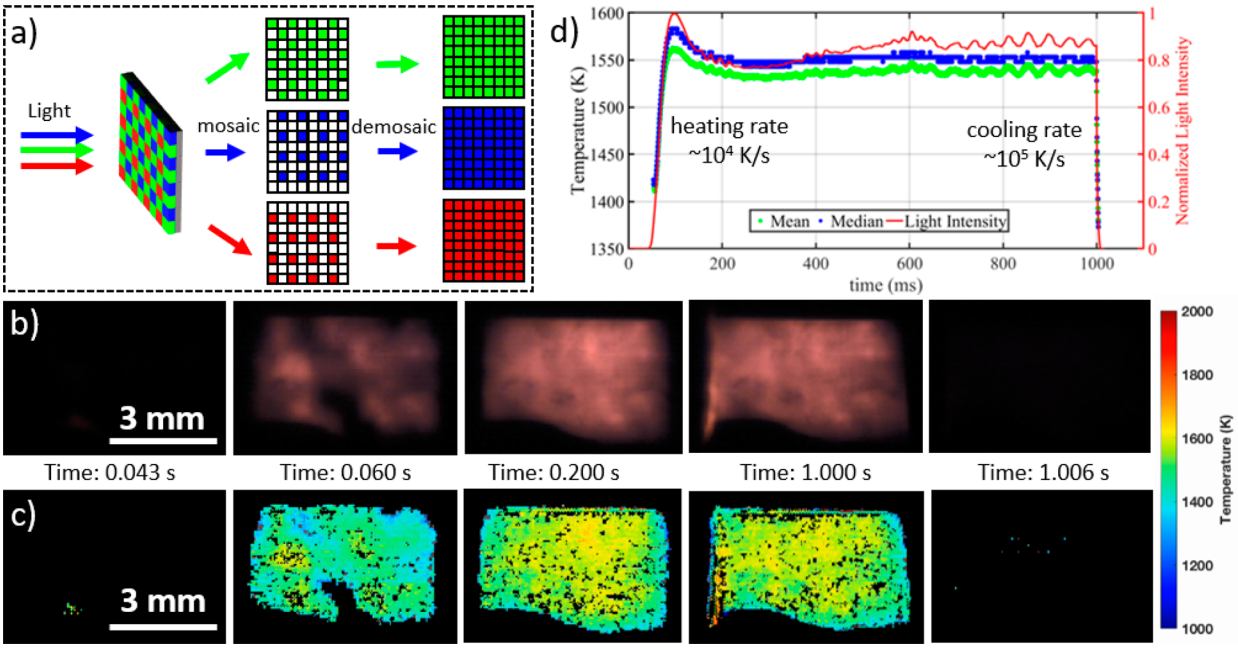

Figure 2. Spatiotemporal temperature mapping: (a) principle of recording a color image with a Bayer filter; (b, c) time-resolved color images of the sample during the laser pulse process and the corresponding time-resolved temperature maps of the sample during the laser pulse process; (d) temperature profile of the thin film sample.

laser beam absorbed by the thin film sample quickly heats the sample to an extremely high temperature (~1550 K), causing thermal decomposition of the precursor and formation of nanoclusters anchored on the carbon nanofibers. Figure 1g depicts that 50 ms laser pulse produces uniformly dispersed Pt nanoclusters with an average diameter of 3.8 nm and a surface number concentration of ~10^{16} #/m^2. Meanwhile, a 1 s laser pulse synthesizes Pt nanoclusters with a larger average diameter of 54 nm and a lower surface number concentration of ~10^{14} #/m^2. An elongated laser pulse accelerates the diffusion small clusters on the carbon nanofiber surface at elevated temperatures, leading to further growth of nanoclusters and a concomitant decrease in their surface density. These results demonstrate that by simply adjusting the pulse duration of the laser pulse, nanoparticles supported on the carbon nanofibers with different size and number density can be generated. Particularly, decreasing the laser pulse duration enables the formation of smaller nanoclusters with higher number densities.

We further investigated the thermal decomposition of metal salt precursor during the rapid heating treatment. Previous thermogravimetric analysis with a slow heating rate (10 K/s) revealed that chloroplatinic acid decomposes to volatile $PtCl_2$ at 415 °C, which further decomposes to metallic Pt at 510 °C:[21]

$$H_2PtCl_6 \xrightarrow{@415\ ^\circ C} PtCl_2 \uparrow + 2HCl \uparrow + Cl_2 \uparrow \xrightarrow{@510\ ^\circ C} Pt + Cl_2\uparrow \quad (5)$$

Temperature-jump/time-of-flight mass spectrometry (T-Jump/TOFMS, see Figure S1) was used to study precursor decomposition under a fast heating rate (10^5 K/s). The principle and details of T-Jump/TOFMS can be found in the Experimental Section and in our previous studies.[22] Briefly, a small amount of metal salt precursor was deposited onto a platinum wire probe. Once loaded into the TOFMS vacuum chamber, the platinum wire probe coated with metal salt precursor was resistively heated by a direct current voltage supply which delivers a rapid heating rate as fast as 10^5 K/s. In this manner, the heating process mimics the heating rate employed in a laser pulse experiment. The mass spectra detected by the TOFMS are shown in Figure S2, confirming the release of volatile $PtCl_2$ during the thermal decomposition of the metal salt precursor. Particularly, $PtCl_2^+$ species was released at a time of 1.1 ms and a temperature of 437 °C, which is comparable to the release temperature of volatile $PtCl_2$ under a slow heating regime (415 °C). Note that the signal intensities for HCl and Cl are much stronger than $PtCl_2$, and no Pt signal was detected by TOFMS. Because the release temperature of $PtCl_2$ is similar under both rapid and slow heating regimes, it is reasonable to believe that volatile $PtCl_2$ was quickly reduced to Pt atoms and recondensed onto a Pt wire at a temperature slightly higher than 510 °C. Heating the sample to even a higher final temperature (1550 K) in an extremely short time further hastens the kinetics of metal salt decomposition and enables the formation of Pt atoms in a relatively short time. The weak signal of $PtCl_2$ also implies its extremely short lifetime under this rapid heating regime. This indicates that $PtCl_2$ is rapidly reduced to Pt atoms, which nucleate and deposit on the surface of the Pt wire. Results from SEM-EDS (Figure S3) further confirm the complete conversion of metal salt precursor to metallic phase particles with a 50 ms laser pulse.

Spatiotemporal Temperature Mapping. The spatiotemporal dynamics of the rapid thermal pulse of the thin film sample induced by the CO_2 laser at high powers was explored by high-speed two-dimensional color camera pyrometry.[20] As shown in Figure 2a, the light signal emitted from the laser-heated CNF thin film first passes through a Bayer mosaic color filter array, which is then used for selective bandpass transmission of light (red, green, and blue). Red, green, or blue sensitivities are recorded by the CMOS sensor of the camera at each pixel, and RGB intensities at each channel are then recovered by

https://dx.doi.org/10.1021/acsanm.0c00238
ACS Appl. Nano Mater. 2020, 3, 2959−2968

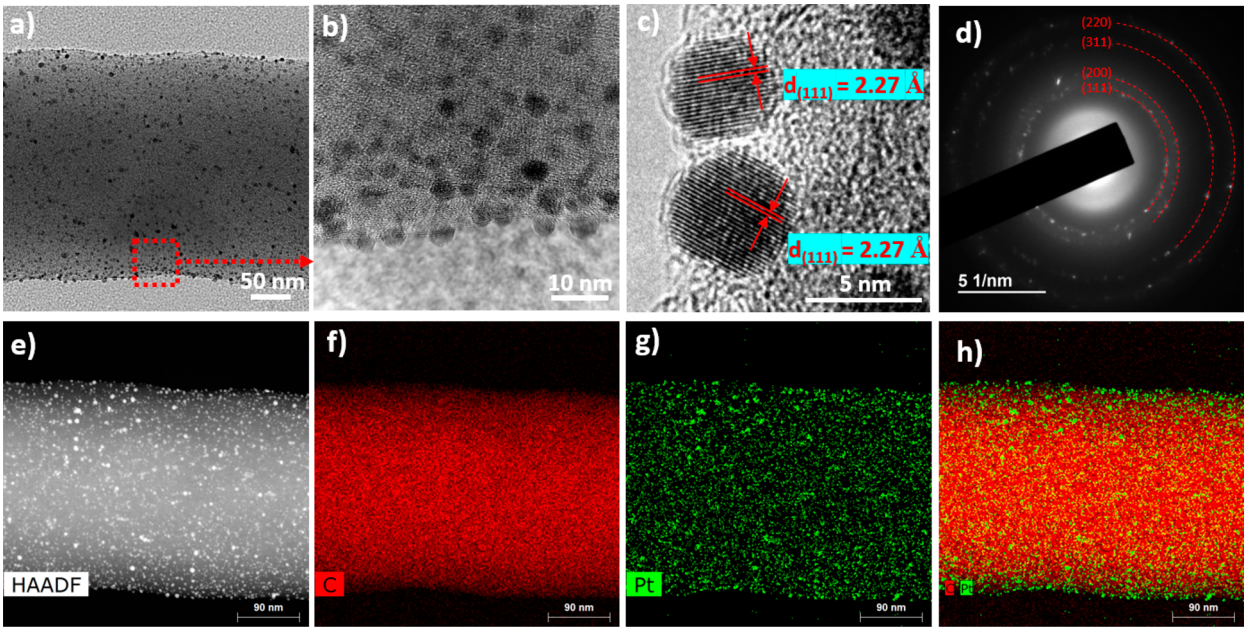

Figure 3. Microstructure analysis of CNF supported Pt nanoclusters synthesized by 50 ms laser-induced thermal pulse. (a−c) TEM images of supported Pt nanoclusters. (d) Selected-area electron diffraction pattern of supported Pt nanoclusters. (e−h) Scanning TEM of supported Pt nanoclusters and their corresponding EDS mappings.

demosaicing the image. The raw channel intensity ratios (green/red, blue/green, and blue/red) are used to determine temperature after appropriate calibration using procedures described previously.[20,23]

The video of the entire laser heating process captured by the color camera and the time-resolved two-dimensional temperature profile of the thin film are shown in the Supporting Information. Figure 2b,c show the snapshot images of the heated sample at selected time points of the 1 s laser pulse and the corresponding temperature maps. The time-resolved temperature maps suggest that the thermal energy provided by laser pulse quickly spreads to the entire film uniformly, leading to an equilibrium temperature of 1550 K in about 50 ms. The uniform temperature distribution in the film is attributed to the high thermal conductivity of the carbon nanofiber matrix. Once the laser pulse was terminated, the thin film sample rapidly cools. The temperature profile of the sample at each time was calculated by averaging all the effective temperature values at each pixel of the two-dimensional temperature map and is shown in Figure 2c. We observe that a 1 s laser pulse irradiated on CNF film renders extremely fast heating (10^4 K/s) and cooling rates (10^5 K/s). The extremely high heating rate rapidly reduces the metal salt to metal atom vapor to build a supersaturated state for nanocluster nucleation. Fast heating and cooling rates were achieved because of the high output power of the laser beam and the small mass of the thin film sample. These rates induced by laser pulse are similar to those achieved via electrical Joule heating and are much higher than those achieved in traditional wet chemistry approaches. Additionally, compared with Joule heating, the laser pulse approach is more amenable to scale-up such as roll-to-roll manufacturing as this approach is not limited to conductive matrices, thus enabling the use of ceramics and polymers.

Microstructural Analysis. The microstructure of CNF supported Pt nanoclusters was examined by transmission electron microscopy (TEM). Figure 3a exhibits Pt nanoclusters stabilized by CNF generated with a 50 ms laser pulse. The TEM image of the labeled area with red dashed square shows that ∼4 nm Pt nanoclusters are uniformly dispersed on CNF with a high surface number density. In particular, there are some particles located right outside of the carbon nanofiber projected area in Figure 3b, indicating that these nanoclusters anchor on the surface of carbon nanofiber instead of being encapsulated inside the nanofiber. This observation is consistent with the morphology of CNF supported nanoclusters shown in the SEM image of Figure 1g. It is observed that most of these nanoclusters (see Figure S4) have a crystalline structure. Even though we do not see any lattice structure for some particles, this might be due to these nanoclusters are out of focus or their crystalline planes are not aligned in a certain way with the electron beam. Besides, the contrast of the nanoclusters with similar size could be different because of their orientation. The high-resolution TEM image in Figure 3c shows that these nanoclusters have a crystalline structure with a *d*-spacing of 2.27 Å, corresponding to the (111) of Pt crystal. The selected-area electron diffraction pattern (SAD) in Figure 3d matches well with that of Pt metal, further confirming the presence of the metallic phase of Pt nanoclusters with a single crystalline structure. It is interesting to note that a crystalline structure is observed even for laser pulse heating with rapid cooling rates (10^5 K/s). This suggests that the crystallization process from liquid Pt droplets occurs faster even at such high cooling rates. Previous studies have shown that a crystallinity can be achieved for liquid iron nanodroplets with a diameter of 10 nm when cooled from 1600 K to room temperature even with a cooling rate as high as 10 K/s.[24] Therefore, the laser pulse approach allows sufficient time for crystallization to occur from liquid Pt droplets.

Figure 3e shows the corresponding scanning transmission electron microscopy (STEM) image of CNF supported metal nanoclusters shown in the TEM image of Figure 3a. Figure 3f−h shows EDS analysis of Pt nanoclusters on the carbon

https://dx.doi.org/10.1021/acsanm.0c00238
ACS Appl. Nano Mater. 2020, 3, 2959−2968

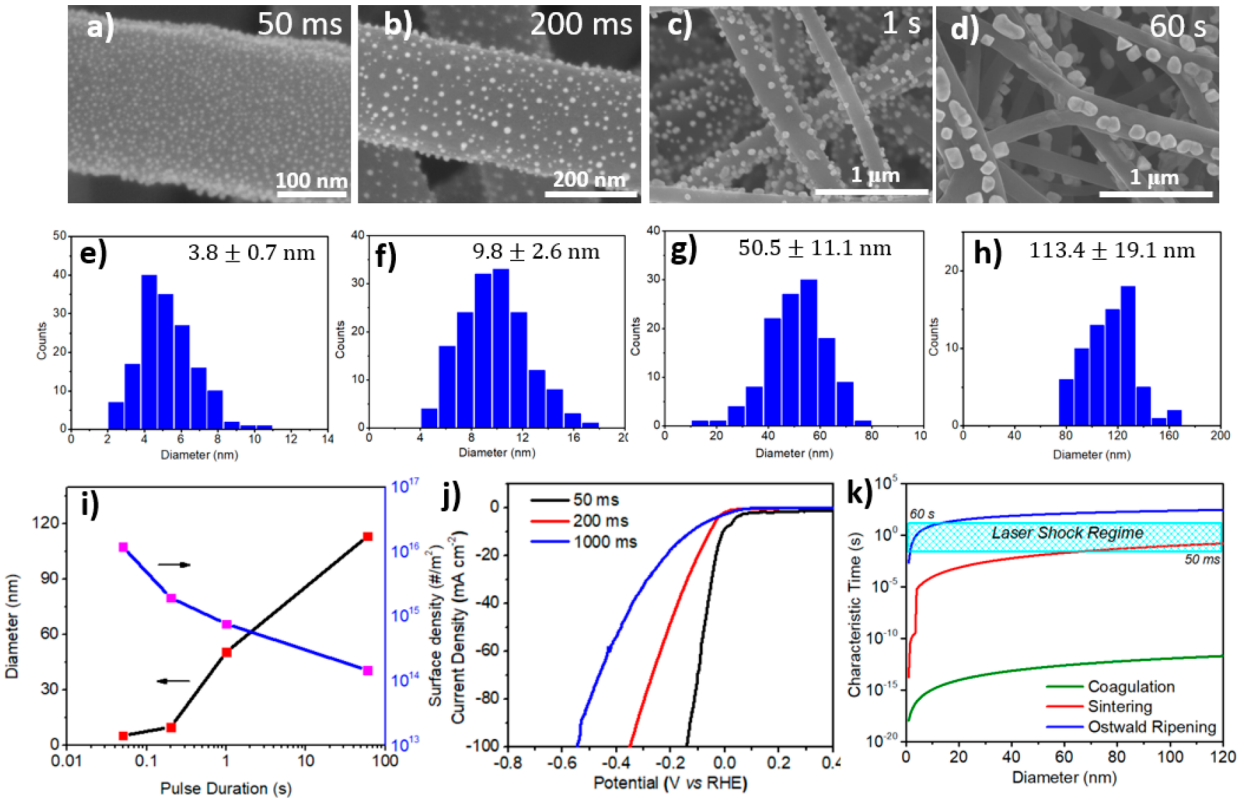

Figure 4. Effect of the duration of laser-induced thermal pulse on the nanocluster size and number density supported on the carbon nanofibers. (a–d) SEM images of metal nanoclusters with different laser pulse pulses (50 ms, 0.2 s, 1 s, and 60 s) and (e–h) their corresponding histograms of size distribution; (i) variations of particle diameter and number density with laser pulse; (j) polarization curve of CNF supported Pt nanoclusters; (k) characteristic times for coagulation, sintering, and Ostwald ripening of monodispersed Pt nanoclusters on the carbon nanofiber surface at 1550 K.

nanofiber. The EDS map for the carbon element shows smooth features, and the edge of the nanofiber is relatively darker because this part is thin and less signal is collected from this area. EDS map for platinum element indicates platinum particles are uniformly distributed on the surface of the carbon nanofiber. It is observed that the height of Pt EDS map is slightly larger than that of the carbon nanofiber matrix, indicating Pt clusters anchoring on the surface of the nanofiber. This observation is further confirmed by the mixed EDS map shown in Figure 3h, which renders bright green edges and no presence of the carbon nanofiber matrix.

We further investigated the effect of the laser pulse duration on nanocluster size and surface number density. The microstructural evolution of Pt nanoclusters with increase of the laser pulse and their corresponding size distribution histograms are shown in Figure 4a–h. The size distributions and the surface density of the nanoclusters were obtained by statistical analysis of SEM images shown in Figure 4a–d. Figure 4i shows that the particle diameter increases with a corresponding decrease in surface number concentration. Longer laser pulses cause further growth of nanoclusters and a decrease in surface density through nanoparticle diffusion and sintering. Interestingly, nanoparticles generated with 1 s laser pulse or smaller are uniformly dispersed on the CNF surface, and no agglomerates are observed. However, nanoparticles are observed to aggregate around the junctions between CNFs, which suggests that particle diffusion might be faster than particle sintering. More detailed analysis on nanoparticle growth mechanism will be explored in the following section.

Interestingly, we observe that increasing laser pulse duration not only leads to a larger particle size but also generates different particle shape and morphology. Figure 4c shows that nanoclusters produced with a 50 ms are primarily spherical in shape. On the other hand, a much longer laser pulse of 60 s generates faceted Pt nanocrystals with a typical octahedral morphology, as shown in Figure S6. Pt nanocrystals with a thermodynamic equilibrium shape are usually bounded by three low-index crystal planes, (100), (110), and (111), with surface tensions following the order $\gamma_{(111)} < \gamma_{(100)} < \gamma_{(110)}$.[25] Pt NPs should therefore take an octahedral shape to maximize the expression of (111) facets and minimize total surface energy. Previous studies have demonstrated the formation of similar 5 nm octahedral platinum nanoparticles by colloidal synthetic routes.[26] However, 5 nm nanoparticles generated with a 50 ms laser pulse have a spherical morphology. This observation can be primarily attributed to the rapid nature of the process which favors the kinetic formation of particles over the thermodynamically favorable morphology. It is well-known that the melting point of metal nanoparticles decreases with their size.[27] At elevated temperatures during laser heating, Pt nanoparticles as small as 5 nm must therefore be in a liquid state. The surface energies for different facets, thus, become similar so that these nanoparticles grow with no preferential facets,[24] resulting in a spherical morphology. Rapid quenching then freezes these spherical nanoparticles and prevents them from reaching the thermodynamically equilibrium shape. For a longer laser pulse, however, the nanoparticles grow into large sizes with their melting point approaching that of bulk Pt. Because the temperatures reached by laser pulse are much

https://dx.doi.org/10.1021/acsanm.0c00238
ACS Appl. Nano Mater. 2020, 3, 2959−2968

lower than bulk melting point of Pt, the surface tension for different facets are energetically distinguishable. These particles, therefore, grow with preferential orientations to stable (111) planes, leading to a thermodynamically equilibrium shape, octahedron.

Example Application. Electricity generated from renewable energy such as solar and wind must be stored durably for off-grid applications. Electrochemical water splitting to produce hydrogen and oxygen provides a promising solution to convert the electrical energy to chemical energy in the form of chemical bonds.[28] Platinum has been proved to be an excellent catalyst to catalyze the reduction of protons to H_2 at high reaction rates and low overpotentials.[29] Here, the electrocatalytic performance of Pt nanoclusters generated with the laser pulse technique toward hydrogen evolution reaction was evaluated. The linear sweep voltammetry polarization curves of the thin film samples treated with different laser pulse durations are shown in Figure 4j. Table S3 summarizes the overpotentials of the three samples at the current densities of 50 mA cm^{-2}. It is clear that the sample with the shortest laser pulse treatment has the best electrocatalytic performance. This is likely because a short laser pulse enables the formation of the smallest nanoclusters with high surface number densities, maximizing the active sites for the electrocatalytic reaction. In particular, the results show that Pt nanoclusters prepared with a 50 ms laser pulse has an overpotential of 76 mV at a current density of 50 mA cm^{-2}. This result is comparable to that of commercial 40 wt % Pt/C composite electrode previously reported,[30] demonstrating promising catalytic performance of the Pt nanoclusters generated with our laser pulse technique.

Nanoparticle Growth Mechanism. Here, we use a simple characteristic time analysis to investigate the likely growth mechanism of nanoclusters on the surface of carbon nanofibers and discuss the role of Brownian coagulation, sintering, and Ostwald ripening on nanocluster formation. In this case, Ostwald ripening describes the process of metal atoms releasing from smaller particles, moving into the gas phase, and attaching onto larger particles.

Consider a CNF thin film matrix with a surface area, A, and a thickness, L, containing uniformly dispersed Pt nanoclusters with a diameter, d_p, and a number concentration, N_0. The number concentration N_0 is correlated to the diameter d_p as follows: $N_0 \propto 1/d_p^3$. The characteristic coagulation time is defined as the time required for the nanoclusters with the initial concentration of N_0 to achieve half of its value. For nanoclusters with a narrow size distribution, the characteristic coagulation time can be estimated by using the following equation:[17]

$$\tau_{coag} = \frac{2}{KN_0} \tag{8}$$

Here, $K = 8\pi D d_p$ is the continuum Brownian coagulation coefficient, where D is the diffusion coefficient of Pt nanoclusters on the surface of the carbon nanofiber. To be in line with previous transport theory, we relate the surface diffusion coefficient D of nanoparticle with the Einstein−Stokes equation of three-dimensional diffusivity, D_∞, by using a hydrodynamic wall-correction factor, λ.[31,32]

$$D = \frac{D_\infty}{\lambda} \tag{9}$$

The Einstein−Stokes equation of the three-dimensional diffusivity, D_∞, is expressed as

$$D_\infty = \frac{kT}{6\pi\eta d_p} \tag{10}$$

where k is the Boltzmann constant, η is the viscosity of air at the temperature T, and d_p is the particle diameter.

We can further estimate the characteristic sintering time for Pt nanoclusters, which is defined as the time required for two contacted primary particles to form a single spherical particle. In our previous study, we have shown that the sintering of metal nanoparticles is sensitive to the phase of the nanoparticles.[27] Our calculation shows that Pt nanoparticles with a diameter of <5.2 nm are in liquid phase at 1550 K. Therefore, a viscous flow mechanism was used to calculate the sintering time of the particles in liquid phase:[33]

$$\tau_{sinter,l} = \frac{\mu d_{eff}}{2\sigma_l} \tag{11}$$

where μ is the viscosity of Pt nanoparticle, σ_l is the surface tension of Pt nanoparticle in the liquid state, d_{eff} is the effective diameter of the sintering particle pair, which is $6V_p/a_p$, and V_p and a_p are volume and surface area of the sintering particle pair, respectively.

For nanoparticles in the solid phase, the sintering time can be estimated as follows:[34]

$$\tau_{sinter,s} = \frac{3k_B TN}{64\pi\sigma_s D_{eff}} \tag{12}$$

where T is the temperature of a particle pair undergoing sintering, N is the number of atoms in the particle pair, σ_s is the surface tension of solid Pt nanoparticle, and D_{eff} is the effective atomic diffusion coefficient of the particle pair.

Another possible mechanism for nanoparticle growth is Ostwald ripening. Ostwald ripening involves the dissolvement of smaller particles and the redeposition of the dissolved species on the surfaces of the larger particles that are far more thermodynamically favorable. The sublimation time is used to estimate the characteristic time for Ostwald ripening. The time to sublime a particle with a diameter of d_p can be derived as[35]

$$\tau_{sublim} = \frac{2B}{A}\left\{E_0\left(\frac{B}{d_p}\right) - E_1\left(\frac{B}{d_p}\right)\right\} \tag{13}$$

where the definition for the constants A, B, $E_0(x)$, and $E_1(x)$ can be found in the Supporting Information. All property data mentioned above can be found in the Supporting Information.

The characteristic times for coagulation, sintering, and Ostwald ripening as a function of nanoparticle diameter are shown in Figure 4k with the laser pulse duration ranging from 50 ms to 60 s. At early stages of nanoparticle growth when the particle size is <10 nm, we observe that all three characteristic times are shorter than the laser pulse duration. This implies that all three growth mechanisms are involved in the initial stages of nanoparticle growth. Small particles diffuse, coagulate, and sinter together to form large particles. Meanwhile, small particles might sublime and disappear, and released metal atoms transport and deposit on relatively larger particles. Once the particles grow to a size of 10 nm and above, the characteristic time for Ostwald ripening becomes longer than the laser pulse duration, suggesting that Ostwald ripening is no

https://dx.doi.org/10.1021/acsanm.0c00238
ACS Appl. Nano Mater. 2020, 3, 2959−2968

longer a dominant force, leaving the primary growth mechanisms as sintering and coagulation. As shown in Figure 4k, the characteristic coagulation time of the Pt nanoparticles is much shorter than the characteristic sintering time, suggesting that we should see the aggregated particles at any stage of particle growth. However, no aggregated particles are observed in the SEM images shown in Figure 4a−c, indicating that particle coagulation on CNF surface might be slower than that demonstrated in Figure 4k. Previous Raman spectrometry analysis on the CNF matrix prepared using a similar procedure has shown that there is relatively strong defect-induced D band, suggesting that there is an abundance of defects on the CNF surface.[5] Molecular dynamics simulations show that these surface defects can provide anchoring sites to stabilize the nanoparticles and significantly retard their diffusion and coagulation on CNF surface.[36] A longer laser pulse (∼60 s) may help remove these defects, which is confirmed by Raman spectrometry result demonstrating no presence of the defect-induced D band for annealed fibers.[5] A decrease in surface defects by laser heating, therefore leads to accelerated diffusion of Pt nanoclusters on CNF surface. This explains the aggregation-dominated formation of larger Pt nanoparticles (Figure 4d) where a 60 s laser pulse was used.

3. CONCLUSIONS

We demonstrate a rapid laser-induced thermal pulse technique to fabricate carbon nanofiber supported ultrasmall metal nanoclusters with high surface density. A rapid laser pulse heating on the metal precursor incorporated CNF matrix triggers fast nucleation and growth of metal nanoclusters, and a subsequent ultrafast quenching freezes them onto the CNF structure. A shorter thermal pulse enables the formation of smaller nanoclusters with higher number densities. A longer thermal pulse enables the further growth of metal nanoparticles and the achievement of their equilibrium shape. A characteristic time analysis suggested that the growth of metal nanoclusters is dominated by coagulation and sintering, and Ostwald ripening is mainly involved at the early stage of nanoparticle formation. As an example of application, we demonstrate very favorable catalytic property of Pt nanoclusters for electrocatalytic hydrogen evolution. This work provides a promising approach for rapid and scalable fabrication of ultrasmall metal nanoclusters and nanocluster-based devices.

4. EXPERIMENTAL SECTION

Carbon Nanofiber (CNF) Preparation. Polyacrylonitrile was added to 10 mL of DMF solvent followed by vigorous stirring overnight. The as-obtained solution was used as the precursor for electrospinning to prepare polyacrylonitrile (PAN) thin film. The precursor solution was loaded into a 10 mL syringe tube and pumped through a flat-top stainless-steel needle (i.d.: 203.2 μm). A pumping rate of 0.5 mL/h, a voltage differential of 12 kV, and a distance of 15 cm between the needle and the aluminum substrate were employed for electrospinning. To prepare CNF films, the as-prepared PAN sample was loaded into a tube furnace, heated to 250 °C with a heating rate of 5 min/°C in the air atmosphere, and kept at 250 °C for 2 h. Then, the sample was heated to 1000 °C with a heating rate of 2 °C/min under H_2/N_2 (v:v = 5:95) atmosphere and kept at 1000 °C for 5 h to obtain CNF thin films.

Metal Salt Loading onto CNF. The metal precursor (0.05 M) was dropped onto carbon nanofiber thin films (2.5 mm × 5.0 mm) using a pipet with a loading of ∼100 μL/cm^2. The metal salt loaded thin film was air-dried. The resulting weight percentage of Pt in CNF matrix is about 30%.

Laser-Induced Thermal Pulse. The metal salt impregnated CNF thin film sample (2.5 mm × 5.0 mm) was mounted on a homemade graphite holder, which was placed in the center of the box chamber filled with inert Ar gas. The freestanding thin film sample was heated by a continuous CO_2 laser, which was controlled by a computer. The duration, output energy power, and the size of the laser beam can be adjusted accordingly. The output power of the laser applied was 90% of the total laser power (80 W). The size of the laser beam was adjusted using a beam expander. In this experiment, the diameter of the laser beam was 4 mm. Therefore, the powder density of the laser beam was ∼400 W/cm^2. The laser pulse process was recorded with a high-speed color camera. The recorded color images were used to extract spatiotemporal temperature of the sample.

Spatiotemporal Temperature Mapping. The temperature of the hot sample is estimated by using eq 1. By taking ratios of raw channel intensities, dependency on most variables associated with intensity is eliminated except for those regarding the channel gain (ψ_i), emissivity (ε), and spectral response (χ_i) of the camera at individual wavelengths and channels.[23] To estimate temperature of the hot surface, the graybody assumption has been modified to account for an optically thin flame by assuming that $\varepsilon \sim 1/\lambda$, substituted into Planck's law, and integrated over the entire spectrum to which the camera is sensitive (as shown in eq 1).[37] When calibrated with a Newport Oriel 67000 Series Blackbody Infrared Light Source, calibration factors C_{gr}, C_{bg}, and C_{br} with data available in the article by Jacob and Kline et al., and these factors were assumed valid from 773 to 4773 K.[20] Through this, calculation of temperature is reduced to matching of calibration factor-corrected channel intensity ratios to theoretical ratios. Three color ratios (green/red, blue/green, and blue/red) were simultaneously used to estimate temperature by minimizing their summed error from theoretical ratios. Further thresholding is used to eliminate summed errors corresponding to a temperature error greater than 110 K. Only unsaturated pixels above the black level and within the error threshold are used to report mean and median temperature of the frame for a contiguous area of at least 10 acceptable pixels.

Catalytic Test. The electrocatalytic performance of the samples toward hydrogen evolution reaction (HER) was tested. The freestanding metal nanoclusters decorated CNF film was directly used as the working electrode. Platinum foil was used as the counter electrode and a standard Ag/AgCl electrode as the reference electrode. HER tests were performed in a 0.5 M H_2SO_4 aqueous solution. The polarization tests were performed by linear sweep voltammetry from 0 to −0.5 V (vs RHE) with a scan rate of 2 mV/s.

Characterization. Morphologies and structures of metal nanoclusters supported on CNF matrix were examined by scanning electron microscopy (SEM, Hitachi SU-70) and transmission electron microscopy (TEM, JEOL JEM 2100 FEG). The mean diameters and size distributions of the nanoparticles were determined by statistical analysis of the acquired TEM images using Nano Measurer 1.2 image analysis software. Particle surface density was also determined by using the acquired TEM image.

■ ASSOCIATED CONTENT

Supporting Information

The Supporting Information is available free of charge at https://pubs.acs.org/doi/10.1021/acsanm.0c00238.

Moment model for saturation ratio calculation; data collected from temperature jump/time of flight mass spectrometry (T-Jump/TOFMS); EDS spectra of metal precursor laden CNF samples before and after 50 ms laser pulse treatment; size-dependent melting point of Pt nanoparticle; property data for characteristic time analysis; high-speed color camera video for temperature measurement; particle density measurement; yield of metal nanoclusters (PDF)

https://dx.doi.org/10.1021/acsanm.0c00238
ACS Appl. Nano Mater. 2020, 3, 2959−2968

Movie S1 (MP4)

■ AUTHOR INFORMATION

Corresponding Authors

Liangbing Hu − *Department of Materials Science and Engineering, University of Maryland, College Park, Maryland 20742, United States;* orcid.org/0000-0002-9456-9315; Email: binghu@umd.edu

Michael R. Zachariah − *Department of Chemical and Environmental Engineering, University of California, Riverside, Riverside, California 92521, United States;* orcid.org/0000-0002-4115-3324; Email: mrz@engr.ucr.edu

Authors

Yong Yang − *Department of Chemical and Biomolecular Engineering, University of Maryland, College Park, Maryland 20742, United States; Department of Chemical and Environmental Engineering, University of California, Riverside, Riverside, California 92521, United States;* orcid.org/0000-0001-5169-1479

Yonggang Yao − *Department of Materials Science and Engineering, University of Maryland, College Park, Maryland 20742, United States*

Dylan J. Kline − *Department of Chemical and Biomolecular Engineering, University of Maryland, College Park, Maryland 20742, United States; Department of Chemical and Environmental Engineering, University of California, Riverside, Riverside, California 92521, United States;* orcid.org/0000-0001-8800-2841

Tangyuan Li − *Department of Materials Science and Engineering, University of Maryland, College Park, Maryland 20742, United States*

Pankaj Ghildiyal − *Department of Chemical and Biomolecular Engineering, University of Maryland, College Park, Maryland 20742, United States; Department of Chemical and Environmental Engineering, University of California, Riverside, Riverside, California 92521, United States*

Haiyang Wang − *Department of Chemical and Environmental Engineering, University of California, Riverside, Riverside, California 92521, United States;* orcid.org/0000-0001-5200-3965

Complete contact information is available at: https://pubs.acs.org/10.1021/acsanm.0c00238

Notes

The authors declare no competing financial interest.

■ ACKNOWLEDGMENTS

This project is supported by an ONR MURI grant and the NSF Scalable Nano- manufacturing Project No. 1635221. Additional recognition is given to the University of Maryland NanoCenter and its AIM lab the use of the SEM/TEM facilities.

■ REFERENCES

(1) Lu, Y.; Chen, W. Sub-nanometre sized metal clusters: from synthetic challenges to the unique property discoveries. *Chem. Soc. Rev.* **2012**, *41* (9), 3594−3623.

(2) Zheng, J.; Yang, Y.; Fan, X.; Ji, G.; Ji, X.; Wang, H.; Hou, S.; Zachariah, M. R.; Wang, C. Extremely stable antimony−carbon composite anodes for potassium-ion batteries. *Energy Environ. Sci.* **2019**, *12* (2), 615−623.

(3) Wang, H.; DeLisio, J. B.; Holdren, S.; Wu, T.; Yang, Y.; Hu, J.; Zachariah, M. R. Mesoporous Silica Spheres Incorporated Aluminum/Poly (Vinylidene Fluoride) for Enhanced Burning Propellants. *Adv. Eng. Mater.* **2018**, *20* (2), 1700547.

(4) Jin, R.; Zeng, C.; Zhou, M.; Chen, Y. Atomically precise colloidal metal nanoclusters and nanoparticles: fundamentals and opportunities. *Chem. Rev.* **2016**, *116* (18), 10346−10413.

(5) Yao, Y.; Huang, Z.; Xie, P.; Lacey, S. D.; Jacob, R. J.; Xie, H.; Chen, F.; Nie, A.; Pu, T.; Rehwoldt, M.; Yu, D.; Zachariah, M. R.; Wang, C.; Shahbazian-Yassar, R.; Li, J.; Hu, L. Carbothermal shock synthesis of high-entropy-alloy nanoparticles. *Science* **2018**, *359* (6383), 1489−1494.

(6) Yao, Y.; Huang, Z.; Xie, P.; Li, T.; Lacey, S. D.; Jiao, M.; Xie, H.; Fu, K. K.; Jacob, R. J.; Kline, D. J.; Yang, Y.; Zachariah, M.; Wang, C.; Shahbazian-Yassar, R.; Hu, L. Ultrafast, Controllable Synthesis of Sub-Nano Metallic Clusters through Defect Engineering. *ACS Appl. Mater. Interfaces* **2019**, *11* (33), 29773−29779.

(7) Davari, S. A.; Gottfried, J. L.; Liu, C.; Ribeiro, E. L.; Duscher, G.; Mukherjee, D. Graphitic coated Al nanoparticles manufactured as superior energetic materials via laser ablation synthesis in organic solvents. *Appl. Surf. Sci.* **2019**, *473*, 156−163.

(8) Muñeton Arboleda, D.; Santillán, J. M.; Mendoza Herrera, L. J.; van Raap, M. B. F. n.; Mendoza Zelis, P.; Muraca, D.; Schinca, D. C.; Scaffardi, L. B. Synthesis of Ni nanoparticles by femtosecond laser ablation in liquids: Structure and sizing. *J. Phys. Chem. C* **2015**, *119* (23), 13184−13193.

(9) Ghildiyal, P.; Yang, Y.; Kline, D. J.; Holdren, S.; Zachariah, M. Ultrafast, Scalable Laser Photothermal Synthesis and Writing of Uniformly-Dispersed Metal Nanoclusters in Polymer Films. *Nanoscale* **2019**, *11*, 13354−13365.

(10) Kunwar, P.; Hassinen, J.; Bautista, G.; Ras, R. H.; Toivonen, J. Direct laser writing of photostable fluorescent silver nanoclusters in polymer films. *ACS Nano* **2014**, *8* (11), 11165−11171.

(11) Oh, Y.; Lee, M. Single-pulse transformation of Ag thin film into nanoparticles via laser-induced dewetting. *Appl. Surf. Sci.* **2017**, *399*, 555−564.

(12) Berean, K. J.; Sivan, V.; Khodasevych, I.; Boes, A.; Della Gaspera, E.; Field, M. R.; Kalantar-Zadeh, K.; Mitchell, A.; Rosengarten, G. Laser-Induced Dewetting for Precise Local Generation of Au Nanostructures for Tunable Solar Absorption. *Adv. Opt. Mater.* **2016**, *4* (8), 1247−1254.

(13) Fowlkes, J. D.; Wu, Y.; Rack, P. D. Directed assembly of bimetallic nanoparticles by pulsed-laser-induced dewetting: a unique time and length scale regime. *ACS Appl. Mater. Interfaces* **2010**, *2* (7), 2153−2161.

(14) Favazza, C.; Kalyanaraman, R.; Sureshkumar, R. Robust nanopatterning by laser-induced dewetting of metal nanofilms. *Nanotechnology* **2006**, *17* (16), 4229.

(15) Henley, S. J.; Watts, P. C.; Mureau, N.; Silva, S. R. P. Laser-induced decoration of carbon nanotubes with metal nanoparticles. *Appl. Phys. A: Mater. Sci. Process.* **2008**, *93* (4), 875−879.

(16) Park, J.; Joo, J.; Kwon, S. G.; Jang, Y.; Hyeon, T. Synthesis of monodisperse spherical nanocrystals. *Angew. Chem., Int. Ed.* **2007**, *46* (25), 4630−4660.

(17) Friedlander, S. K. *Smoke, Dust, and Haze: Fundamentals of Aerosol Dynamics*; Topics in Chemical Engineering; Oxford University Press: New York, 2000.

(18) Yang, Y.; Ghildiyal, P.; Zachariah, M. R. Thermal Shock Synthesis of Metal Nanoclusters within On-the-Fly Graphene Particles. *Langmuir* **2019**, *35* (9), 3413−3420.

(19) Anumol, E. A.; Kundu, P.; Deshpande, P. A.; Madras, G.; Ravishankar, N. New insights into selective heterogeneous nucleation of metal nanoparticles on oxides by microwave-assisted reduction: rapid synthesis of high-activity supported catalysts. *ACS Nano* **2011**, *5* (10), 8049−8061.

(20) Jacob, R. J.; Kline, D. J.; Zachariah, M. R. High speed 2-dimensional temperature measurements of nanothermite composites: Probing thermal vs. Gas generation effects. *J. Appl. Phys.* **2018**, *123* (11), 115902.

(21) Schweizer, A.; Kerr, G. Thermal decomposition of hexachloroplatinic acid. *Inorg. Chem.* **1978**, *17* (8), 2326−2327.
(22) Rehwoldt, M. C.; Yang, Y.; Wang, H.; Holdren, S.; Zachariah, M. R. Ignition of Nanoscale Titanium/Potassium Perchlorate Pyrotechnic Powder: Reaction Mechanism Study. *J. Phys. Chem. C* **2018**, *122* (20), 10792−10800.
(23) Densmore, J. M.; Biss, M. M.; McNesby, K. L.; Homan, B. E. High-speed digital color imaging pyrometry. *Appl. Opt.* **2011**, *50* (17), 2659−2665.
(24) Zhao, J.; Baibuz, E.; Vernieres, J.; Grammatikopoulos, P.; Jansson, V.; Nagel, M.; Steinhauer, S.; Sowwan, M.; Kuronen, A.; Nordlund, K.; Djurabekova, F. Formation mechanism of Fe nanocubes by magnetron sputtering inert gas condensation. *ACS Nano* **2016**, *10* (4), 4684−4694.
(25) Peng, Z.; Yang, H. Designer platinum nanoparticles: Control of shape, composition in alloy, nanostructure and electrocatalytic property. *Nano Today* **2009**, *4* (2), 143−164.
(26) Tao, A. R.; Habas, S.; Yang, P. Shape control of colloidal metal nanocrystals. *Small* **2008**, *4* (3), 310−325.
(27) Yang, Y.; Romano, M.; Feng, G.; Wang, X.; Wu, T.; Holdren, S.; Zachariah, M. R. Growth of Sub-5 nm Metal Nanoclusters in Polymer Melt Aerosol Droplets. *Langmuir* **2018**, *34* (2), 585−594.
(28) Gao, M.-R.; Liang, J.-X.; Zheng, Y.-R.; Xu, Y.-F.; Jiang, J.; Gao, Q.; Li, J.; Yu, S.-H. An efficient molybdenum disulfide/cobalt diselenide hybrid catalyst for electrochemical hydrogen generation. *Nat. Commun.* **2015**, *6*, 5982.
(29) Wei, H.; Huang, K.; Wang, D.; Zhang, R.; Ge, B.; Ma, J.; Wen, B.; Zhang, S.; Li, Q.; Lei, M.; Zhang, C.; Irawan, J.; Liu, L.-M.; Wu, H. Iced photochemical reduction to synthesize atomically dispersed metals by suppressing nanocrystal growth. *Nat. Commun.* **2017**, *8* (1), 1490.
(30) Li, Y.; Gao, T.; Yao, Y.; Liu, Z.; Kuang, Y.; Chen, C.; Song, J.; Xu, S.; Hitz, E. M.; Liu, B.; Jacob, R. J.; Zachariah, M. R.; Wang, G.; Hu, L. In Situ "Chainmail Catalyst" Assembly in Low-Tortuosity, Hierarchical Carbon Frameworks for Efficient and Stable Hydrogen Generation. *Adv. Energy Mater.* **2018**, *8* (25), 1801289.
(31) Feitosa, M.; Mesquita, O. Wall-drag effect on diffusion of colloidal particles near surfaces: a photon correlation study. *Phys. Rev. A: At., Mol., Opt. Phys.* **1991**, *44* (10), 6677.
(32) Davis, A. M.; Kezirian, M. T.; Brenner, H. On the Stokes-Einstein model of surface diffusion along solid surfaces: Slip boundary conditions. *J. Colloid Interface Sci.* **1994**, *165* (1), 129−140.
(33) Mukherjee, D.; Sonwane, C.; Zachariah, M. Kinetic Monte Carlo simulation of the effect of coalescence energy release on the size and shape evolution of nanoparticles grown as an aerosol. *J. Chem. Phys.* **2003**, *119* (6), 3391−3404.
(34) Wu, M.; Windeler, R.; Steiner, C.; Börs, T.; Friedlander, S. Controlled synthesis of nanosized particles by aerosol processes. *Aerosol Sci. Technol.* **1993**, *19* (4), 527−548.
(35) Asoro, M. A.; Kovar, D.; Ferreira, P. J. In situ transmission electron microscopy observations of sublimation in silver nanoparticles. *ACS Nano* **2013**, *7* (9), 7844−7852.
(36) Chen, Y.; Egan, G. C.; Wan, J.; Zhu, S.; Jacob, R. J.; Zhou, W.; Dai, J.; Wang, Y.; Danner, V. A.; Yao, Y.; Fu, K.; Wang, Y.; Bao, W.; Li, T.; Zachariah, M. R.; Hu, L. Ultra-fast self-assembly and stabilization of reactive nanoparticles in reduced graphene oxide films. *Nat. Commun.* **2016**, *7*, 12332.
(37) Kalman, J.; Hedman, T. On the Origin and Use of the Emissivity Approximations for Alumina Particles. *Propellants, Explos., Pyrotech.* **2016**, *41* (5), 793−797.

https://dx.doi.org/10.1021/acsanm.0c00238
ACS Appl. Nano Mater. 2020, 3, 2959−2968